

# Non-linear Dynamic Characteristics of High-Speed Wheel-Rail Interface Considering Surface Topography and Liquid Medium

Huifang Xiao, Zhaoxin Liu and Jingjiang Zhang

School of Mechanical Engineering, University of Science and Technology Beijing, Beijing 100083, PR China.

E-mail: huifangxiao@ustb.edu.cn

(Received 16 February 2023; accepted 28 June 2023)

In this work, the force-deflection characteristics, and the nonlinear vibration of the wheel-rail interaction with surface roughness and liquid medium are studied. The statistical micro-contact Greenwood and Williamson model is used to characterize the rough surface. The load sharing theory is used to determine the analytical elastic contact force-deflection and damping force-deflection relationships, which are further approximated by power law functions. The nonlinear contact stiffness and damping characteristics are illustrated for different rough surface topographies and running speeds. The natural frequency is solved by assuming small covariates and defining time variables of different scales. Effects of surface topography and liquid medium on the natural frequency of the wheel-rail interface system are studied. The first-order harmonic responses under harmonic excitation are further determined as well as the jump-up and jump-down responses for different rough surface topographies, excitation loads, liquid mediums and running speeds. It is shown that the resonance region and the peak value of the vibration amplitude increase as the surface roughness, running speed and excitation load increase; whilst the jump-up and jump-down frequencies decrease. In addition, the system can change from a monostable to a bistable structure when surface roughness and excitation force increase and large limit cycle oscillation can occur.

## NOMENCLATURE

$E_1, E_2, E$	Elastic modulus of wheel, Elastic modulus of rail, Equivalent elastic modulus	$\gamma_1, \gamma_2$	Load sharing factors of liquid medium and micro-asperities
$\nu_1, \nu_2$	Poisson's ratio of wheel and rail, respectively	$N$	Total number of asperities
$h$	Film thickness	$f_e$	Elastic contact force of a single asperity
$d_d$	Distance between the average height of the rough surface and the mean line of height for micro convex body	$n_d$	Asperity distribution density
$z_b$	Distance between the top of a single micro convex body and the mean line of height of micro convex body	$A_n$	Nominal contact area
$z_0$	Distance between the mean height of the initial rough surface and the rail plane	$\phi_n(z_n)$	Probability density function of Gaussian distribution
$w$	Deformation of a single micro convex body	$\sigma$	Standard deviation of the surface heights distribution
$z_a$	Wheel-rail contact deformation	$G$	Dimensionless material parameter
$R$	Radius of wheel	$W$	Dimensionless load
$m$	Weight of wheel	$L$	Contact length
$u$	Wheel speed	$\mu_0$	Inlet viscosity
$\beta$	Radius of a sphere on a rough surface	$\kappa$	Pressure-viscosity coefficient
$k_1$	Equivalent stiffness of suspension system	$\rho$	Liquid density
$c_1$	Damping coefficient of the suspension system	$\alpha$	Stiffness index
$\delta$	Equivalent static deformation of wheel-rail contact interface	$k$	Stiffness coefficient
$P_0$	Axle load	$C_t$	Total contact damping coefficient of wheel-rail interface
$z$	Displacement of the wheel relative to the static equilibrium position	$C_l$	Normal contact damping coefficient of the liquid part
$F_k$	Non-linear elastic force	$C_a$	Normal contact damping coefficient of the solid part
$F_d$	Non-linear damping force	$\eta_e$	Loss factor
$F_e$	Amplitude of the harmonic load	$K_a$	Normal contact stiffness of the solid part
$F_h, F_a$	Normal contact force of the liquid part and the solid part, respectively	$A_a$	Contact area of the solid part
		$c$	Damping coefficient
		$n$	Damping index
		$b$	Constant value of damping
		$\omega_s$	Undamped natural frequency
		$\beta_n$	Non-linear stiffness rate
		$\Omega_0$	Dimensionless natural frequency

$S_0$	Initial displacement
$S_1$	Primary resonance response amplitude
$S_2$	Amplitude of the second-order harmonic response
$\Omega$	Dimensionless excitation frequency
$F_n$	Dimensionless excitation load

## 1. INTRODUCTION

The wheel-rail relationship is critical in railway transportation, which is closely related to the dynamics and stable operation of high-speed trains.<sup>1</sup> The wheel-rail interface is very susceptible to wear and tear, thus causing peeling, scuffing and other defects, resulting in wheel and rail surfaces with different degrees of roughness.<sup>2</sup> At the same time, as an open tribological system, the wheel-rail contact is subjected to different kinds of environmental influences, such as oil, rain, snow, and leaves. The wheel-rail interface has the characteristics of rough surface topography and a liquid medium, which each have a significant influence on the contact stiffness, damping and the frequency responses of the system.<sup>3-5</sup> Therefore, it is necessary to study the contact characteristics and the dynamic performances of high-speed wheel-rail contact considering the interface properties of surface topography and a liquid medium.

The contact characteristics of the wheel-rail interface with surface roughness and liquid medium are receiving increased attention. Xie et al.<sup>6</sup> investigated the railhead wear in respect to surface roughness growth based on a time-domain wheel-track vertical interaction model. The wheel-rail contact was modelled with a non-linear Hertzian contact spring in which the surface roughness amplitude was included in the deformation. Rovira et al.<sup>7</sup> developed a methodology to predict the wear performance of wheel-rail contact by combining the experimental measurements and the Hertzian contact model. The effect of the surface roughness was included in the experimental measurement of the surface profile and the contact profile was fitted using an equivalent ellipse. The Hertzian contact was assumed for the interaction of the wheel-rail pair. However, the liquid medium between the wheel-rail contact was neglected in these models.

The liquid medium at the wheel-rail interface is further considered to study the contact interaction and wear/adhesion performance of wheel-rail contact by using both experimental methods and model predictions.<sup>8-13</sup> Water is mostly introduced as the medium at the wheel-rail interface, where studies have examined the influence of water on contact behavior. For example, Baek et al.<sup>14</sup> used a twin-disc-type of rolling-sliding frictional machine to simulate the wheel-rail contact under low slip ratio and low rolling speed. The effects of rolling speed, contact pressure and environmental variables of temperature and relative humidity on the traction characteristics were investigated. Liu et al.<sup>15</sup> measured the lateral adhesion ratio under dry and wet conditions, and the results show that the lateral adhesion ratio decreases after the application of water. Considering the falling leaves and oil at the rail, other liquid mediums at the wheel-rail interface are also considered in addition to water. For example, Rong et al.<sup>16</sup> investigated the effect of ambient humidity on the adhesion between the wheel-rail interface with the twin-disc test rig considering different lubrication mediums of water, leaf juice and oil. Galas et al.<sup>17</sup> used a ball-on-disc tribometer with a climate chamber to simulate

the rolling-sliding contact under various environmental conditions with clean and leaf extract-contaminated discs. Wu et al.<sup>18-20</sup> established a preliminary numerical model of wheel-rail in rolling contact to study the adhesion characteristics of wheel-rail considering surface roughness under oil and water mixed contamination.

Although non-linear interaction models of wheel-rail contact with surface roughness and liquid medium have been developed to predict wear/adhesion performance, the current models are established with the surface roughness modeled using Hertzian contact and the influences of surface roughness and liquid medium on contact surface stiffness and damping being ignored. In addition, the previous studies mainly focused on the wear/adhesion characteristics of the wheel-rail interface in condition of surface roughness and liquid medium. The influences of wheel-rail interface properties on the vibration dynamic performances of the wheel-rail system are not concerned. The purpose of this work is to develop an engineering approach to predict the contact stiffness and damping characteristics at the wheel-rail interface with surface roughness and a liquid medium and to further study the dynamic responses of the wheel-rail system. The rough surface is characterized using the statistical micro-contact Greenwood and Williamson (GW) model,<sup>21</sup> in which the statistical parameters are used to represent the surface profile, such as the standard deviation of the surface heights distribution and asperity distribution density. The empirical film thickness equation for mixed lubrication contact is employed together with the contact pressure equations to predict the film thickness, and the loads supported by the micro asperities and liquid film, based on the idea that the vertical load of wheel-rail interface is shared by the micro asperities and a liquid medium. It is therefore both convenient and more applicable to practical engineering to analyse the effect of surface roughness and a liquid medium on the performances. The elastic contact force-deflection and the damping force-deflection are determined and are further approximated using power law function. The natural frequency is solved by assuming small covariates and defining time variables of different scales. The first-order harmonic responses under harmonic excitation are also determined. The influence of the wheel-rail surface roughness, liquid medium, excitation load and running speed on the nonlinear contact stiffness and damping characteristics are studied, as well as for the natural frequency and the frequency responses of the wheel-rail contact system.

## 2. DYNAMIC MODEL

The wheel-rail contact is an open-air system. Different environmental factors can affect the characteristics of the wheel-rail interface, such as the presence of water, fallen leaves and oil, as shown in Fig. 1. The surface of the wheel track is rough and covered with liquid and leaves.

The rough surface can be characterized using the statistical micro-contact GW model, as shown in Fig. 2. The GW model proposed by Greenwood and Williamson assumes that the surface roughness is isotropic, and the asperities are in elastic contact. The tip of the convex body can be regarded as a sphere with the same curvature radius  $\beta$  and the height following a Gaussian distribution. The contact area between the wheel and the rail are filled with liquid and leaves. The elastic modulus

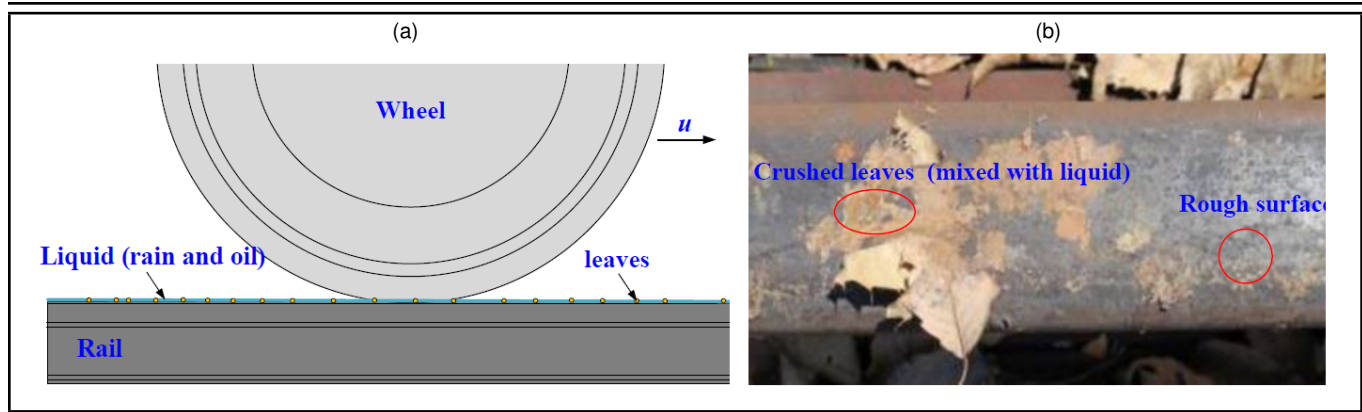


**Figure 1.** (a) The wheel-rail contact with surface roughness and liquid medium, (b) the track surface.<sup>4</sup>

and the Poisson's ratio of the wheel and rail are  $E_1$  and  $E_2$ ,  $\nu_1$  and  $\nu_2$ , respectively. The equivalent elastic modulus of the wheel is  $2/E = (1 - \nu_1^2)/E_1 + (1 - \nu_2^2)/E_2$ . The distance between the mean height of the initial rough surface and the rail plane is  $z_0$ . The wheel is squeezed on the rigid plane under the action of its own gravity and external load, resulting in the deformation  $z_a$ . The distance between the average height of the rough surface after deformation and the mean line of height of the asperities is  $d_d$ . The distance between the top of a single asperity and the mean line of height of asperities is  $z_b$ . The deformation of a single asperity is  $w = z_b + d_d - h$ . In addition, the wheel rolls along the rail at speed  $u$ , allowing the lubricant to enter the contact area. The film thickness  $h$  is the distance between the average height of the deformed rough surface and the rigid plane with  $h = z_0 - z_a$ .

During high-speed operation, the rough surface and liquid medium between the wheel and the track affect the dynamic characteristics of the wheel-rail interface. In order to investigate the nonlinear dynamics of the wheel-rail interface, the dynamic model of the wheel-rail interface is established as shown in Fig. 3. The contact is equivalent to a spring-damped system with non-linear elastic force  $F_k$  and non-linear damping force  $F_d$  to characterize the influence of the wheel-rail surface roughness and the third medium on the contact system. The wheelset, with mass  $m$  and radius  $R$ , and the suspension on the wheel form a spring-weight-damped vibration system with stiffness  $k_1$  and damping  $c_1$ . Under the action of axle weight  $P_0$ , the static equilibrium position of the contact interface vibration system changes to  $\delta$ . In addition, the wheel moving forward at speed  $u$  is excited by the irregularity vertical excitation of the wheel-rail contact surface and generates contact vibration. The displacement of the wheel relative to the static equilibrium position is  $z = z_a - \delta$ , and  $z_a$  is the contact deformation of the wheel and rail.

The wheel-rail interface is stimulated by wheel polygon wear and rail irregularities and can be considered as a periodic external harmonic excitation.<sup>23</sup> Therefore, the dynamic equation for the contact vibration near the static equilibrium position of the wheel-rail system can be expressed as

$$m\ddot{z} + c_1\dot{z} + k_1(z + \delta) + F_k(z + \delta) + F_d(z + \delta) - mg - P_0 = F_e \cos(\omega t); \quad (1)$$

where  $m$  is the mass of the wheelset,  $c_1$  and  $k_1$  are damping ratio and stiffness of the suspension system, respectively,  $F_k$  is the non-linear elastic force,  $F_d$  is the non-linear damping

force,  $F_e$  is the amplitude of the harmonic external excitation,  $\omega$  is the excitation frequency.

As seen, to obtain the dynamic responses of the wheel-rail interface, it is necessary to determine the nonlinear elastic force  $F_k$  and the nonlinear damping force of the wheel-rail interface firstly.

### 3. FORCE-DEFLECTION CHARACTERISTICS OF THE WHEEL-RAIL INTERFACE WITH ROUGH TOPOGRAPHY AND LIQUID MEDIUM

#### 3.1. Elastic Force-Deflection Characteristics

Considering the rough topography and liquid medium at the wheel-rail interface, according to the load sharing theory,<sup>8</sup> the vertical loads on the wheel and rail are borne by the micro asperities and the liquid medium. Deformations of asperities and liquid medium are both generated. Consequently, the non-linear elastic force  $F_k$  can be expressed as

$$F_k = F_h + F_a; \quad (2)$$

where  $F_h$  was the normal contact force of the liquid part,  $F_a$  was the normal contact force of the solid part. The relationship between  $F_h$  and  $F_a$  can be expressed as  $F_h = F_k/\gamma_1$  and  $F_a = F_k/\gamma_2$ ,  $\gamma_1$  was the load sharing factors of the liquid medium,  $\gamma_2$  was the load sharing factors of the micro-asperities at the wheel-rail interface, which have the relationship

$$\frac{1}{\gamma_1} + \frac{1}{\gamma_2} = 1. \quad (3)$$

The load sharing factors can vary for different surface roughness values and lubrication states.<sup>24</sup>

According to the GW statistical contact model, the normal contact force  $F_a$  of the solid asperities can be determined as<sup>25</sup>

$$F_a = N \int_{h-d_d}^{\infty} f_e \phi(z_b) dz_b; \quad (4)$$

where  $N$  was the total number of asperities with  $N = n_d A_n$ ,  $n_d$  was the asperity distribution density,  $A_n$  was the nominal contact area,  $f_e$  was the elastic contact force of a single asperity at the wheel-rail interface with  $f_e = 2/3 E \beta^{1/2} w^{2/3}$ ,  $\beta$  was the curvature radius of the asperities,  $w$  was the deflection with

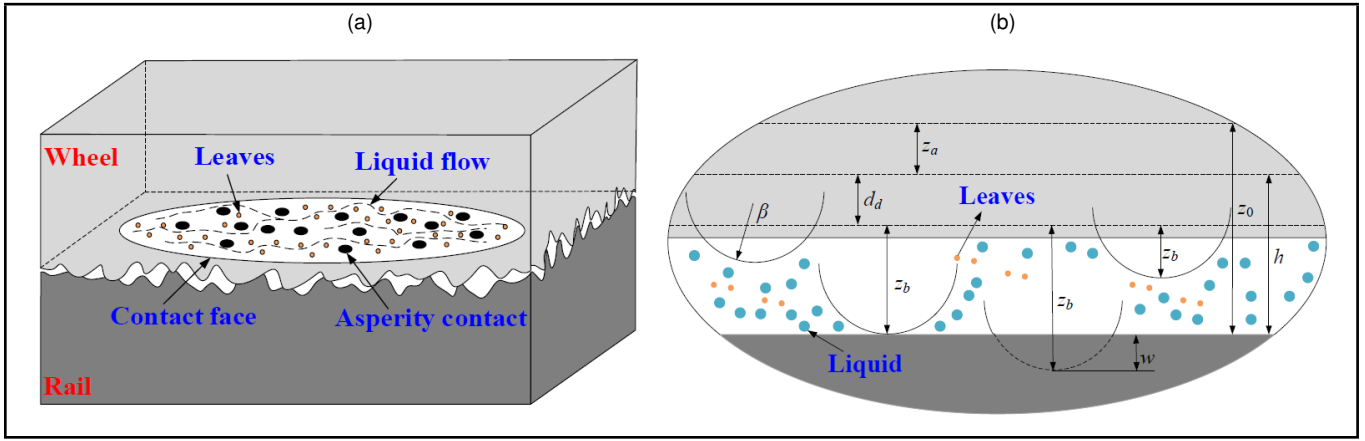


Figure 2. Schematic diagram of the contact model for rough wheel-rail interface: (a) wheel-rail contact model, (b) micro-contact model.<sup>22</sup>

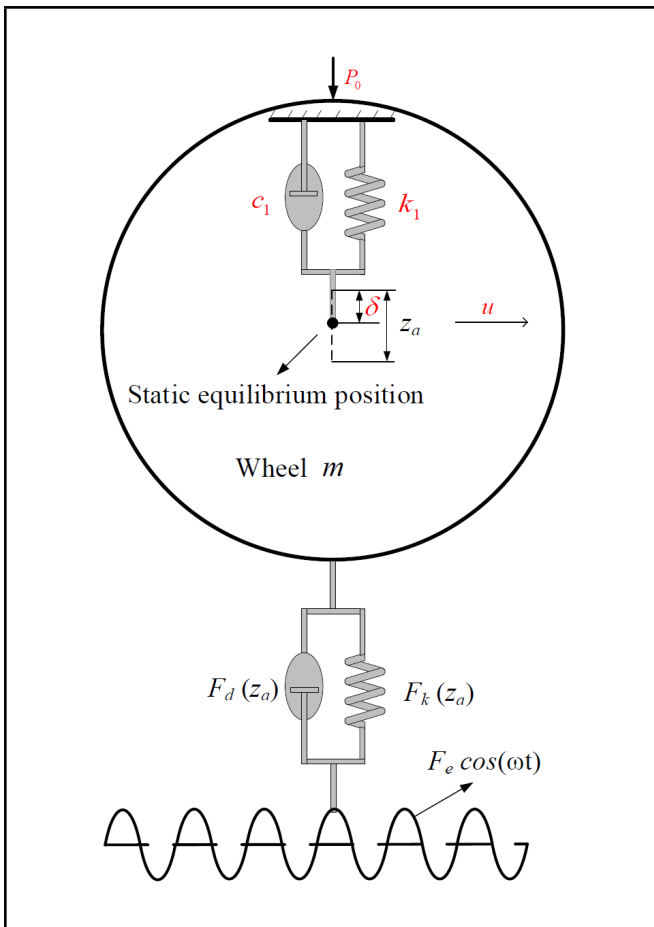


Figure 3. Vertical dynamic model of the wheel-rail interface.

$w = z_b + d_d - h$ ,  $\phi(z_b)$  is the probability density function of height distribution following the Gaussian distribution with

$$\phi(z_b) = 1/\sqrt{2\pi}(\sigma/\sigma_s)e^{[-1/2(z/\sigma_s)^2]}; \quad (5)$$

where  $\sigma$  was the standard deviation of the surface heights distribution,  $\sigma_s$  was the standard deviation of asperity heights distribution, and the relationship between the two can be expressed as  $\sigma/\sigma_s = n_d\beta\sigma / ((n_d\beta\sigma)^2 - 3.71693 \times 10^{-4})^{1/2}$ .<sup>26</sup>

Combining Eqs. (4) and (5), and introducing the following dimensionless parameters:  $z_n = z_b/\sigma$ ,  $h_n = h/\sigma$ ,  $d_n = d_d/\sigma$ ,  $\phi(z_n) = 1/\sqrt{2\pi}(\sigma/\sigma_s)e^{[-1/2(\sigma/\sigma_s)^2 z_n^2]}$ ; the di-

mensionless nonlinear elastic force  $F_k$  can be obtained as

$$F_k(h_n) = \frac{2}{3}n_d\gamma_2 A_n E \beta^{1/2} \sigma^{1/2} \int_{h_n-d_n}^{\infty} (z_n+d_n-h_n)^{3/2} \phi_n(z_n) dz_n, \\ h_n = \frac{z_0 - y - \delta}{\delta}; \quad (6)$$

where  $h$  was the film thickness,  $\phi_n(z_n)$  is the normalized probability density function of height distribution.

Equation (6) shows that the non-linear elastic force is the function of the interface film thickness. Assuming that the film thickness in the entire contact area is constant and equal to the central film thickness, considering the influence of surface roughness and load sharing, the film thickness under mixed lubrication can be obtained as<sup>22</sup>

$$\bar{h} = \left[ \gamma_1^{3/2} \left( H_{RI}^{7/3} + \gamma_1^{-14/15} H_{EI}^{7/3} \right)^{3/7} + \gamma_1^{-5/2} \left( H_{RP}^{-7/2} + H_{EP}^{-7/2} \right)^{-2/7} \right]^{1/5} \sqrt{U\gamma_1}; \quad (7)$$

where

$$s = \frac{7 + 8e^{-2\gamma_1^{-2/5} \left( \frac{-2H_{EI}}{H_{RI}} \right)}}{5}. \quad (8)$$

The dimensionless parameters are

$$M = WU^{-1/2}, \quad W = \frac{F_k}{ERL}, \quad U = \frac{\mu_0}{\mu}, \quad Q = GU^{1/4}, \\ G = \kappa E, \quad \bar{h} = \frac{h}{R}, \quad H_{RI} = 3M^{-1}, \quad H_{EI} = 2.621M^{-1/5}, \\ H_{RP} = 1.287Q^{2/3}, \quad H_{EP} = 1.311M^{-1/8}Q^{3/4}; \quad (9)$$

where  $G$  was a dimensionless material parameter,  $W$  was the dimensionless load,  $R$  was the equivalent radius of the cylinder,  $L$  was the contact length,  $\mu_0$  was the inlet viscosity (viscosity at the ambient pressure),  $u$  was the relative interfacial motion at the contact region,  $\kappa$  is the pressure-viscosity coefficient.

Equation (6) has two unknown quantities:  $\gamma_2$  and  $h$ . To determine the unknown parameters, we need another equation. Combining the center contact pressure of the rough line contact<sup>27</sup> and the contact pressure of the rough surface in the GW

**Table 1.** Parameters used in calculation.<sup>20, 28, 29</sup>

Parameters	Values
$R$ (m)	0.43
$E_1, E_2$ (Pa)	$2.06 \times 10^{11}$
$v_1, v_2$	0.3
$P_0$ (t)	14
$\mu_0$ (Pa·s)	0.08 (oil), 0.00103 (water)
$\rho$ (kg/m <sup>3</sup> )	870 (oil), 1000 (water)
$m$ (kg)	413
$A_n$ (m <sup>2</sup> )	0.01

model, the equation can be obtained as

$$\left[1 + \left(a_1 n_g^{a_2} \sigma_{sn}^{a_3} W^{a_2 - a_3} \gamma_2^{a_2}\right)^{a_4}\right]^{1/a_4} \frac{1}{\gamma_2} = \frac{2}{3} n_g \sigma_{sn}^{3/2} \bar{F}_k F_{3/2} \left(\frac{\bar{h} - \bar{d}}{\sigma_{sn}}\right); \quad (10)$$

where  $a_1 = 1.558$ ,  $a_2 = 0.0337$ ,  $a_3 = -0.442$ ,  $a_4 = -1.70$  and the dimensionless parameters are

$$n_g = n_d R \sqrt{\beta R}, \quad \sigma_{sn} = \frac{\sigma_s}{R}, \quad \bar{F}_k = \sqrt{\frac{2\pi L R E}{F_k}}, \quad \bar{d} = \frac{d_d}{R},$$

$$F_{3/2} \left(\frac{h - d_d}{\sigma_s}\right) = \int_{(h-d_d)/\sigma_s}^{\infty} \left(z_b - \frac{h-d_d}{\sigma_s}\right)^{3/2} \frac{1}{\sqrt{2\pi}} e^{-z^2/2} dz_b. \quad (11)$$

Combining Eqs. (3), (7) and (10), the film thickness  $h$ , the load sharing factor of liquid medium  $\gamma_1$  and the load sharing factor of solid part  $\gamma_2$  can be solved. The main input data used in calculation are listed in Table 1. Figure 4 shows the predicted variation of load sharing factor with velocity for different surface roughness values. The load ratio of liquid medium increases with velocity and exhibits a larger value for surface with a smoother topography, which also shows a more rapid increase. The load ratio of solid part decreases accordingly.

The relationship between the elastic force and the normal deformation at the wheel-rail interface are calculated for different surface roughness and different operating speeds, as shown in Fig. 5. The elastic contact force increases nonlinearly with the deflection and can be approximated as a power function to represent the complicated expression of Eq. (6). The approximated relationship is expressed as

$$F_k(z_a) = k z_a^\alpha, \quad z_a = z_0 - h; \quad (12)$$

where  $\alpha$  was the stiffness index,  $z_a$  is the normal deformation, the stiffness coefficient  $k$  depends on the surface roughness and material properties. The fitted curves using Eq. (12) are also shown in Fig. 5. It can be seen that Eq. (12) can accurately characterize the original relationship between the non-linear elastic force and the normal deformation. The parameters of the fitted expression are illustrated in Table 2. The values of both  $k$  and  $\alpha$  increase for rougher surfaces and higher running speeds.

### 3.2. Damping Force-Deflection Characteristics

To obtain the dynamic responses of the wheel-rail interface, it is also necessary to solve the damping force of the interface.

**Table 2.** Parameters of the fitted expression between elastic force and deformation.

Velocity $u$ (km/h)	Roughness $\sigma$ ( $\mu\text{m}$ )	$k$	$\alpha$
200	0.2	$6.366 \times 10^{29}$	3.655
200	0.3	$3.872 \times 10^{30}$	3.796
200	0.4	$8.914 \times 10^{31}$	4.076
200	0.5	$2.933 \times 10^{32}$	4.220
100	0.4	$1.163 \times 10^{28}$	3.438
150	0.4	$7.840 \times 10^{29}$	3.736
200	0.4	$8.914 \times 10^{31}$	4.076
250	0.4	$9.805 \times 10^{33}$	4.422

Assuming the contact damping between the wheel-rail interface is equivalent to viscous damping, the damping force can be expressed as

$$F_d = C_t \dot{z}_a, \quad z_a = z_0 - h; \quad (13)$$

where  $C_t$  was the total contact damping coefficient of the wheel-rail interface in mixed lubrication. It can be expressed as

$$C_t = C_a + C_l; \quad (14)$$

where  $C_a$  was the damping coefficient of the solid part and  $C_l$  was the damping coefficient of the liquid part.

The damping coefficient of the solid part at the wheel-rail interface can be expressed as

$$C_a = \eta_c \sqrt{m K_a}; \quad (15)$$

where  $\eta_c$  was the loss factor,  $m$  is the mass of the wheelset, and  $K_a$  is the normal contact stiffness of the solid part. The liquid damping coefficient can be expressed as<sup>30</sup>

$$C_l = \frac{3}{5} \frac{(A_n - A_a)^3}{A_a} \frac{\mu_0}{\pi h^3}; \quad (16)$$

where  $A_a$  was the contact area of the solid part.

Combining Eqs. (14), (15) and (16), the total damping coefficient  $C_t$  of the normal contact between the wheel and rail interface is obtained as

$$C_t = \eta_c \sqrt{m K_a} + \frac{3}{5} \frac{(A_n - A_a)^3}{A_a} \frac{\mu_0}{\pi h^3}. \quad (17)$$

The relationship between the total damping coefficient and the normal deformation at the wheel-rail interface under different surface roughness and different operating speeds are calculated and shown in Fig. 6. The total damping coefficient decrease nonlinearly with the deflection. Similarly, the total damping coefficient of the wheel-rail interface can be also approximated using a power law function as

$$C_t = c z_a^n + b; \quad (18)$$

where  $c$  was the damping coefficient,  $n$  was the damping index,  $b$  was the constant. The approximated curves between the total damping coefficient and the normal deflection as also shown in Fig. 6. Equation (18) can accurately characterize the relationship of the original damping coefficient and deflection. Table 3 shows the values of parameters  $c$ ,  $n$  and  $b$  in Eq. (18) for the surface roughness and running speed considered. The values of both  $c$  and  $n$  increase for rougher surfaces and higher running speeds; whilst the value of  $b$  is opposite.

Substituting Eq. (18) into Eq. (13), the approximated non-linear damping force can be expressed as

$$F_d(x) = (c z_a^n + b) \dot{z}_a, \quad Z_a = z + \delta. \quad (19)$$

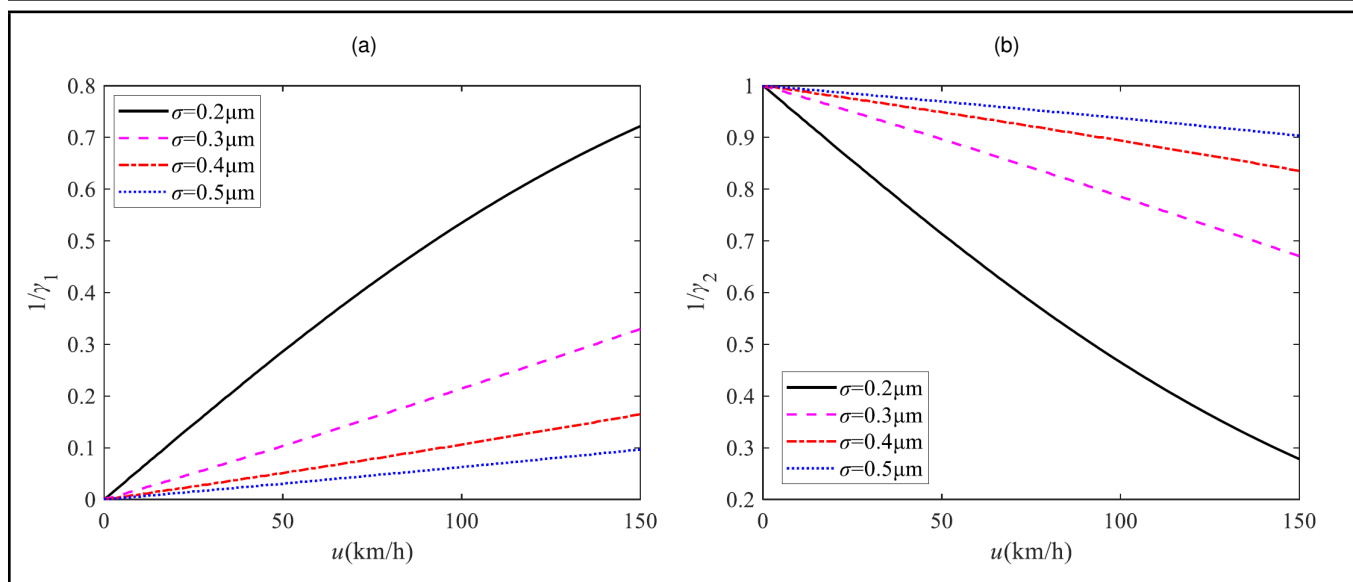


Figure 4. The relationship between load ratio and speed for different surface roughness: (a) load ratio of liquid medium, (b) load ratio of solid part.

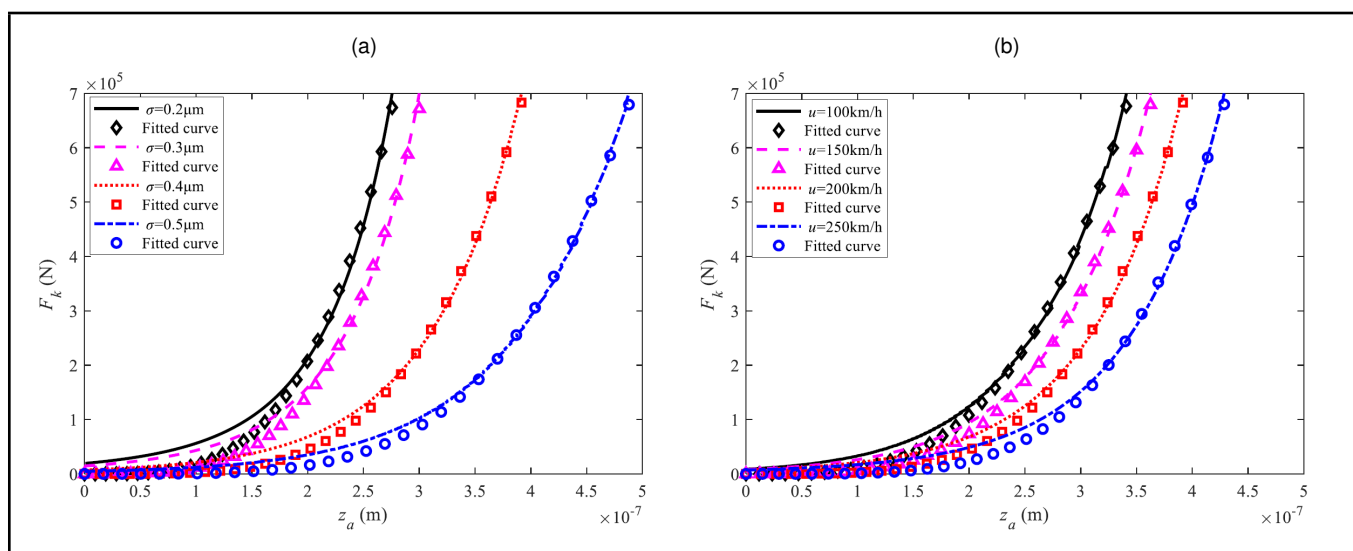


Figure 5. The relationship between non-linear elastic force and normal deformation: (a) different roughness values with  $u = 200$  km/h, (b) different running speeds with  $\sigma = 0.4 \mu\text{m}$ .

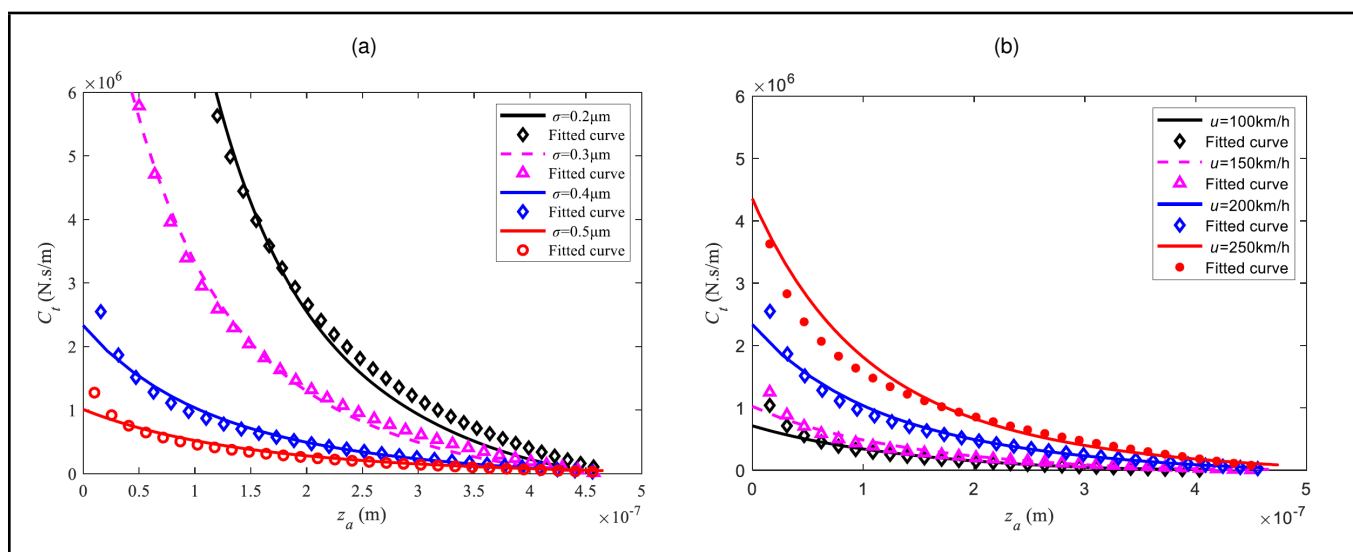


Figure 6. The relationship between total damping coefficient and normal deformation: (a) different roughness values with  $u = 200$  km/h, (b) different running speeds with  $\sigma = 0.4 \mu\text{m}$ .

**Table 3.** Parameters of the expression between total damping coefficient and deflection.

Velocity $u$ (km/h)	Roughness $\sigma$ ( $\mu\text{m}$ )	$c$	$n$	$b$
200	0.2	2.379	-0.9408	$-2.088 \times 10^6$
200	0.3	394.5	-0.5893	$-2.133 \times 10^6$
200	0.4	$9.171 \times 10^4$	-0.2204	$-2.263 \times 10^6$
200	0.5	$4.761 \times 10^5$	-0.1102	$-2.351 \times 10^6$
100	0.4	2921	-0.3481	$-4.868 \times 10^5$
150	0.4	9370	-0.2973	$-7.15 \times 10^5$
200	0.4	$9.171 \times 10^4$	-0.2204	$-2.263 \times 10^6$
250	0.4	$4.931 \times 10^6$	-0.06912	$-1.346 \times 10^7$

The approximated expressions for contact elastic force and damping force of Eqs. (12) and (19) are then substituted into the dynamic Eq. (1) for further calculation.

### 4. DYNAMIC PERFORMANCE OF THE WHEEL-RAIL INTERFACE SYSTEM

Substituting Eqs. (12) and (19) into Eq. (1), the dynamic equation of the wheel-rail interface system can be expressed as

$$m\ddot{z} + c_1\dot{z} + k_1(z + \delta) + k(z + \delta)^\alpha + [c(z + \delta)^n + b]\dot{z} - mg - P_0 = F_e \cos(\omega t). \quad (20)$$

Equation (20) has the exponent nonlinearity and it is difficult to solve the equation analytically. To obtain the analytical solution of Eq. (20), a third-order Taylor expansion is performed on the non-linear elastic force at the static equilibrium point, keeping the smaller series and ignoring the higher-order terms, and introducing the following dimensionless parameters

$$Z = \frac{z}{\delta}, \quad \Omega = \frac{\omega}{\omega_s}, \quad \zeta_1 = \frac{c_1 + b}{2m\omega_s}, \quad \zeta_2 = \frac{c\delta^n}{2m\omega_s}, \quad F = \frac{F_e}{m\omega_s^2\delta}; \quad (21)$$

where  $\Omega_s$  was the undamped natural frequency at the static equilibrium position with  $\omega_s = \sqrt{k(\delta)/m}$ ,  $k(\delta)$  was the stiffness at static equilibrium  $\delta$ . Substituting the time scale  $\tau = \omega_s t$  into Eq. (20), the equation can be rewritten as

$$\ddot{Z} + 2\zeta_1\dot{Z} + 2\zeta_2(Z + 1)^n\dot{Z} + Z + \frac{\alpha - 1}{2}\beta Z^2 + \frac{(\alpha - 1)(\alpha - 2)}{6}\beta Z^3 = F \cos(\Omega\tau); \quad (22)$$

where the non-linear stiffness rate was  $\beta_n = \frac{\alpha k \delta^{\alpha-1}}{k_1 + \alpha k \delta^{\alpha-1}}$ , which represented the proportion of the non-linear stiffness caused by the rough topography and liquid medium of the wheel-rail interface to the total stiffness of the system. Since the stiffness  $k_1$  was much smaller than stiffness  $k$ , the non-linear stiffness rate  $\beta_n$  was seen as unity as  $\beta_n = 1$ .

#### 4.1. Natural Frequency

In this section, the natural frequency of the wheel-rail interface system is studied. The undamped free vibration equation of the wheel-rail contact interface can be obtained by setting  $\zeta_1 = 0, \zeta_2 = 0, F = 0$  and Eq. (22) is rewritten as

$$\ddot{Z} + Z + \frac{\alpha - 1}{2}Z^2 + \frac{(\alpha - 1)(\alpha - 2)}{6}Z^3 = 0. \quad (23)$$

Equation (23) can be solved using the multi-scale method (MMS).<sup>31</sup> Assuming small covariates  $\varepsilon$  and defining time variables of different scales  $T_\alpha = \varepsilon^\alpha t, \alpha = 0, 1, 2, \dots$

$$\frac{d}{dt} = \frac{dT_0}{dt} \frac{\partial}{\partial T_0} + \frac{dT_1}{dt} \frac{\partial}{\partial T_1} + \dots = D_0 + \varepsilon D_1 + \dots;$$

$$\frac{d^2}{dt^2} = D_0^2 + 2\varepsilon D_0 D_1 + \varepsilon^2 (D_1 + 2D_0 D_2) + \dots \quad (24)$$

Assuming the solution of Eq. (23) is

$$Z(t, \varepsilon) = \varepsilon Z_1(T_0, T_1, T_2) + \varepsilon^2 Z_2(T_0, T_1, T_2) + \varepsilon^3 Z_3(T_0, T_1, T_2) + \dots \quad (25)$$

Substituting Eqs. (24) and (25) into Eq. (23) and making the coefficients of  $\varepsilon, \varepsilon^2$  and  $\varepsilon^3$  equal

$$D_0^2 Z_1 + Z_1 = 0; \quad (26)$$

$$D_0^2 Z_2 + Z_2 = -2D_0 D_1 Z_2 - \frac{\alpha - 1}{2} Z_1^2; \quad (27)$$

$$D_0^2 Z_3 + Z_3 = -2D_0 D_1 Z_2 - D_1^2 Z_1 - 2D_0 D_2 Z_1 - (\alpha - 1) Z_1 Z_2 - \frac{(\alpha - 1)(\alpha - 2)}{6} Z_1^3. \quad (28)$$

Assuming the solution of Eq. (26) is

$$Z_1 = A(T_1, T_2)e^{iT_0} + \bar{A}(T_1, T_2)e^{-iT_0}. \quad (29)$$

Substituting Eq. (29) into Eq. (27) gives

$$D_0^2 Z_2 + Z_2 = -2iD_1 A e^{iT_0} - \frac{\alpha - 1}{2} (A^2 e^{2iT_0} + A\bar{A}) + cc; \quad (30)$$

where  $cc$  is the conjugate, the solution of Eq. (30) can be expressed as

$$Z_2 = \frac{\alpha - 1}{6} A^2 e^{2iT_0} - \frac{\alpha - 1}{2} A\bar{A} + cc. \quad (31)$$

Substituting Eqs. (29) and (31) into Eq. (28) gives

$$2iD_2 A + \frac{3(\alpha - 1)(\alpha - 1) - 5(\alpha - 1)^2}{6} A^2 \bar{A} = 0. \quad (32)$$

Assuming

$$A = \frac{1}{2} a_n e^{i\varphi}; \quad (33)$$

where  $a_n$  and  $\varphi$  are functions of  $T_2$ .

Substituting Eq. (34) into Eq. (33) and separating the real and imaginary parts

$$\varphi = \frac{3(\alpha - 1)(\alpha - 2) - 5(\alpha - 1)^2}{24} a_n^2 T_2 + \varphi_0; \quad (34)$$

where  $\varphi_0$  is a constant. Substituting Eqs. (29), (31), (33) and (34) into Eq. (25) gives

$$Z = \varepsilon a_n \cos(\Omega_0 t + \varphi_0) - \frac{\varepsilon^2 a_n^2 (\alpha - 1)}{4} \times \left[ 1 - \frac{1}{3} \cos(2\Omega_0 t + 2\varphi_0) \right] + o(\varepsilon^2); \quad (35)$$

where  $\Omega_0$  was the natural frequency. When the dimensionless initial condition was  $Z(0) = Z_0, Z'(0) = 0, \varphi_0 = 0$  and the natural frequency is expressed as

$$\Omega_0 = 1 + \left[ \frac{3(\alpha - 1)(\alpha - 2) - 5(\alpha - 1)^2}{48} \right] \times \left[ 1 + \frac{\alpha - 1}{6} Z_0 \right]^2 Z_0^2; \quad (36)$$

where  $Z_0$  was the initial displacement.

The relationship between the natural frequency  $\Omega_0$  of the wheel-rail contact system and the initial displacement  $Z_0$  under different surface roughness and liquid mediums is shown in Fig. 7. In Fig. 7(a), the roughness values are  $\sigma = 0.2 \mu\text{m}$ ,  $0.3 \mu\text{m}$ ,  $0.4 \mu\text{m}$  and  $0.5 \mu\text{m}$ , and  $\sigma/R$  was taken to represent the dimensionless roughness. For the linear system, the stiffness index was  $\alpha = 1$ . In Fig. 7(b), three different liquid mediums of water, leaf juice and oil were considered. The viscosity and density of leaf juice were the intermediate values of water and oil.<sup>4,32</sup> When  $u = 200 \text{ km/h}$  and  $\sigma = 0.4 \mu\text{m}$ , the values of stiffness index  $\alpha$  for water, leaf juice and oil were obtained as  $\alpha = 3.796$ ,  $\alpha = 3.166$  and  $\alpha = 2.318$ . Figure 7 shows that for the linear system, the natural frequency is independent of the initial conditions of the system, and its value is always unity. For the non-linear wheel-rail contact system, the initial displacement has an obvious influence on the natural frequency. The maximum value of natural frequency for the wheel-rail contact vibration system appeared at the static equilibrium position  $Z_0 = 0$ , and the natural frequency decreased with the increase of initial displacement. The variation of natural frequency increased with the wheel-rail interface roughness. The natural frequency also changed with liquid medium. The variation of natural frequency with water is the largest, followed by leaf juice, and oil exhibits the smallest.

## 4.2. Forced Vibration Response

In this section, the forced vibration responses of the wheel-rail contact interface under harmonic excitation are analysed for different operating speeds, surface roughness, excitation loads and liquid mediums. The fourth order Runge-Kutta method was used to solve Eq. (22) for the steady-state solution. Figure 8 shows examples of the frequency spectrum obtained using Fourier transformation on the steady-state solutions. Both first order and second order harmonic spectrums were clearly observed. Accordingly, the approximate solution of the dynamic equation can be expressed as

$$Z = S_0 + S_1 \cos(\Omega\tau) + S_2 \cos(2\Omega\tau); \quad (37)$$

where  $S_0$  was the balance position offset,  $S_1$  was the amplitude of the first-order harmonic response,  $S_2$  was the amplitude of the second-order harmonic response, and  $\Omega$  was the dimensionless excitation frequency.

For different excitation frequencies and system parameters, the steady-state time series responses of the forced vibration Eq. (18) can be predicted using the fourth order Runge-Kutta method. The amplitude of the first-order harmonic response  $S_1$  can be extracted by nonlinear fitting the responses. The relationship between the amplitude of the first-order harmonic response  $S_1$  and the excitation frequency  $\Omega$  is shown in Fig. 9 for different operating speeds and surface roughness. The system was a monostable structure and shows the nonlinear characteristics of gradual softening. As the surface roughness and speed increase, the resonance region, and the peak value of the vibration amplitude increase. The rougher the surface of the wheel track, the greater the nonlinearity of the amplitude frequency response curve. The jump-up and jump-down phenomenon is also observed. When the excitation frequency increases, the response amplitude jumps abruptly to a larger value; when the frequency decreases, the response amplitude jumps to a

smaller value. As the surface roughness and speed increases, the jump-up and jump-down frequencies decreases.

The relationship between the amplitude of the first-order harmonic response  $S_1$  and the excitation frequency  $\Omega$  is shown in Fig. 10 for different surface roughness and excitation force  $F_n = F_e/mg$ . Figures 10(a), (b) and (c) show that for surface with smaller roughness, the system is a monostable structure and exhibits a gradually softening nonlinear characteristic. As the excitation load increase, the jump-up and jump-down frequencies of monostable structure decrease. Figure 10(d) shows that for surface with larger roughness and increased excitation force, i.e.,  $F_n \geq 1.06$ , the system transits from monostable structure to bistable structure. It turns to the large limit cycle oscillation of the bistable structure with  $S_1 > 0.6$ . The amplitude of the large limit cycle oscillation increases with the frequency. At the same time, when the excitation load increases, the frequency bandwidth and amplitude of large limit cycle oscillation increases. For  $S_1 < 0.6$ , it is in the small limit cycle oscillation. The primary amplitude-frequency response curves of small limit cycle oscillation are like the primary amplitude-frequency response curves of monostable structure. The jump-up and jump-down phenomenon is also observed when the system is a bistable structure. As the excitation load increase, the jump-up frequency of bistable structure decrease, the jump-down frequency of bistable structure increases.

The relationship between the amplitude of the first-order harmonic response  $S_1$  and the excitation frequency  $\Omega$  is shown in Fig. 11 for different surface roughness and liquid mediums. Three different liquid mediums of water, leaf juice and oil are considered. The system is a monostable structure and exhibits a gradually softening nonlinear characteristic. The resonance region and peak value of vibration for medium water exhibit the largest, followed by leaf juice, and oil has the smallest value. At the same time, the jump-up and jump-down frequencies with oil is the largest, followed by leaf juice, and water exhibits the smallest.

## 5. CONCLUSIONS

In this work, the force-deflection characteristics and the nonlinear vibration of the wheel-rail interaction with surface roughness and liquid medium are studied based on the statistical micro-contact model of the rough surface and load sharing concept. The rough surface is characterized using the statistical GW model and the empirical film thickness equation for mixed lubrication contact is employed together to predict the film thickness and loads supported by the micro-asperities and liquid film. The nonlinear elastic contact force-deflection and the damping force-deflection relationships are derived and approximated using power law functions. The natural frequency is determined using the multiple scales method on the approximate equation. It has been shown that the variation of natural frequency increases with the surface roughness. As for the effect of liquid medium, the variation of natural frequency with oil is the largest, followed by medium leaf juice and water. The first-order harmonic responses under harmonic excitation are also determined as well as the jump-up and jump-down responses. Effects of surface roughness, operating speed, lubrication medium and excitation force amplitude on the nonlinear vibration responses of the system are also presented. It is noted that the current study assumes the isothermal operat-

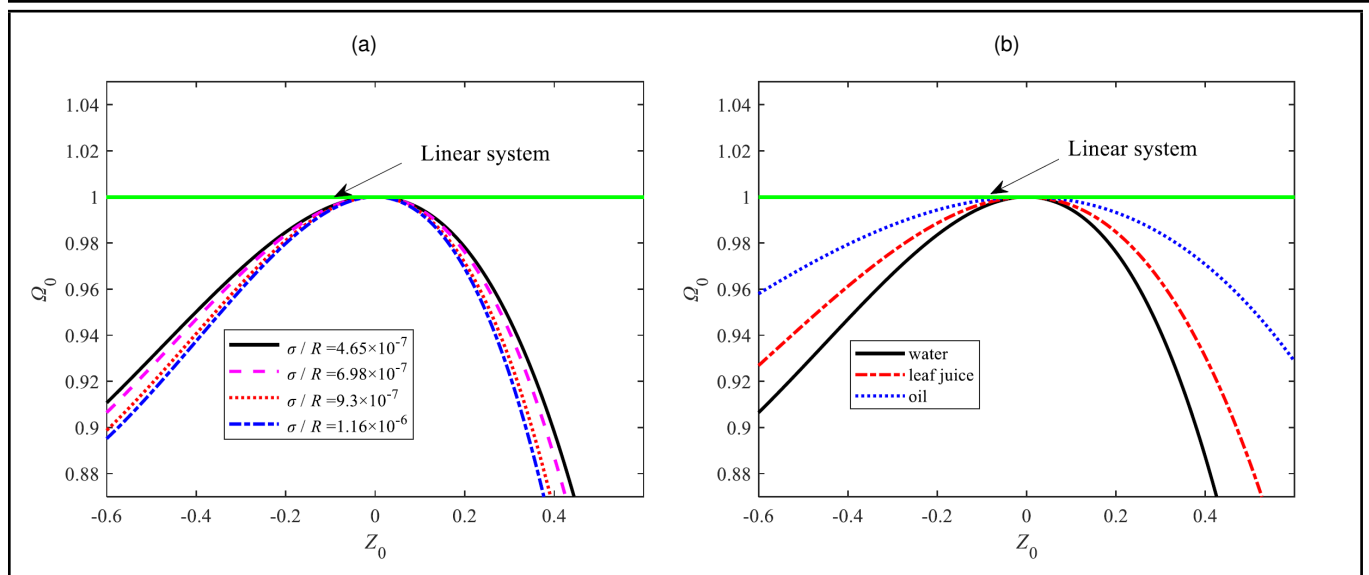


**Figure 7.** The variation of dimensionless natural frequency for wheel-rail interface with dimensionless initial displacement: (a) different roughness values, (b) different liquid mediums.

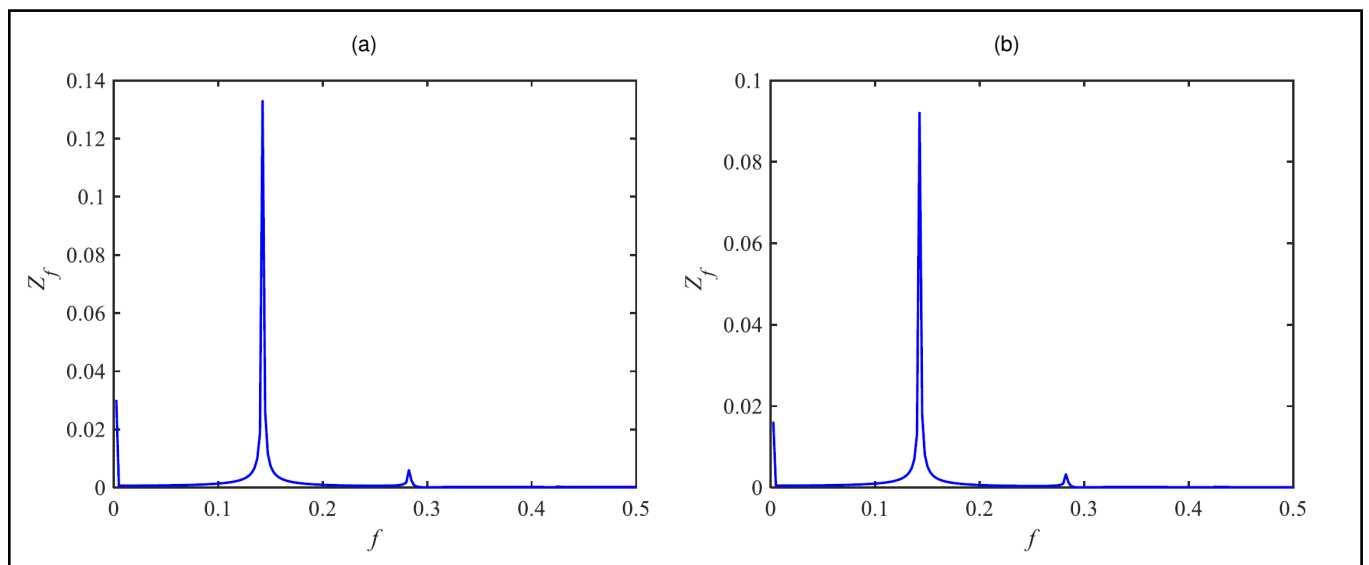


**Figure 8.** The frequency spectrums of the time domain responses for: (a)  $\sigma/R = 9.3 \times 10^{-7}$ ,  $U = 5.7 \times 10^{-13}$ ,  $\Omega = 0.88$ , (b)  $\sigma/R = 9.3 \times 10^{-7}$ ,  $U = 7.1 \times 10^{-13}$ ,  $\Omega = 0.88$ .

ing condition. As the train operates, heat is generated and film temperature will rise, which will result in reduction of lubricant viscosity and film thickness and further influence the load sharing ratios and force-deflection characteristics. Moreover, the influence of tangential motion at the wheel-rail interface on the normal contact interactions are ignored in the current work. This may be further studied in future research.

**ACKNOWLEDGEMENT**

This work was supported by the National Natural Science Foundation of China [grant number 52275081, 51775037]; Open Project Foundation of the State Key Laboratory of Traction Power in Southwest Jiaotong University [grant number TPL2307].

**REFERENCES**

<sup>1</sup> Li, C., Liu, W., and Liang, R. Identification of vertical wheel-rail contact force based on an analytical model

and measurement and its application in predicting ground-borne vibration, *Measurement*, **186**, 110182, (2021). <https://doi.org/10.1016/j.measurement.2021.110182>

<sup>2</sup> Xiao, G., Wu, B., Yao, L., and Shen, Q. The traction behaviour of high-speed train under low adhesion condition, *Engineering Failure Analysis*, **131**, 105858, (2022). <https://doi.org/10.1016/j.engfailanal.2021.105858>

<sup>3</sup> Xiao, H., Shao, Y., and Brennan, M. J. On the contact stiffness and nonlinear vibration of an elastic body with a rough surface in contact with a rigid flat surface, *European Journal of Mechanics—A/Solids*, **49**, 321–328, (2015). <https://doi.org/10.1016/j.euromechsol.2014.08.005>

<sup>4</sup> Chen, H., Furuya, T., Fukagai, S., Saga, S., and Suzumura, J. Wheel slip/slide and low adhesion caused by fallen leaves, *Wear*, 446–447, 203187, (2020). <https://doi.org/10.1016/j.wear.2020.203187>

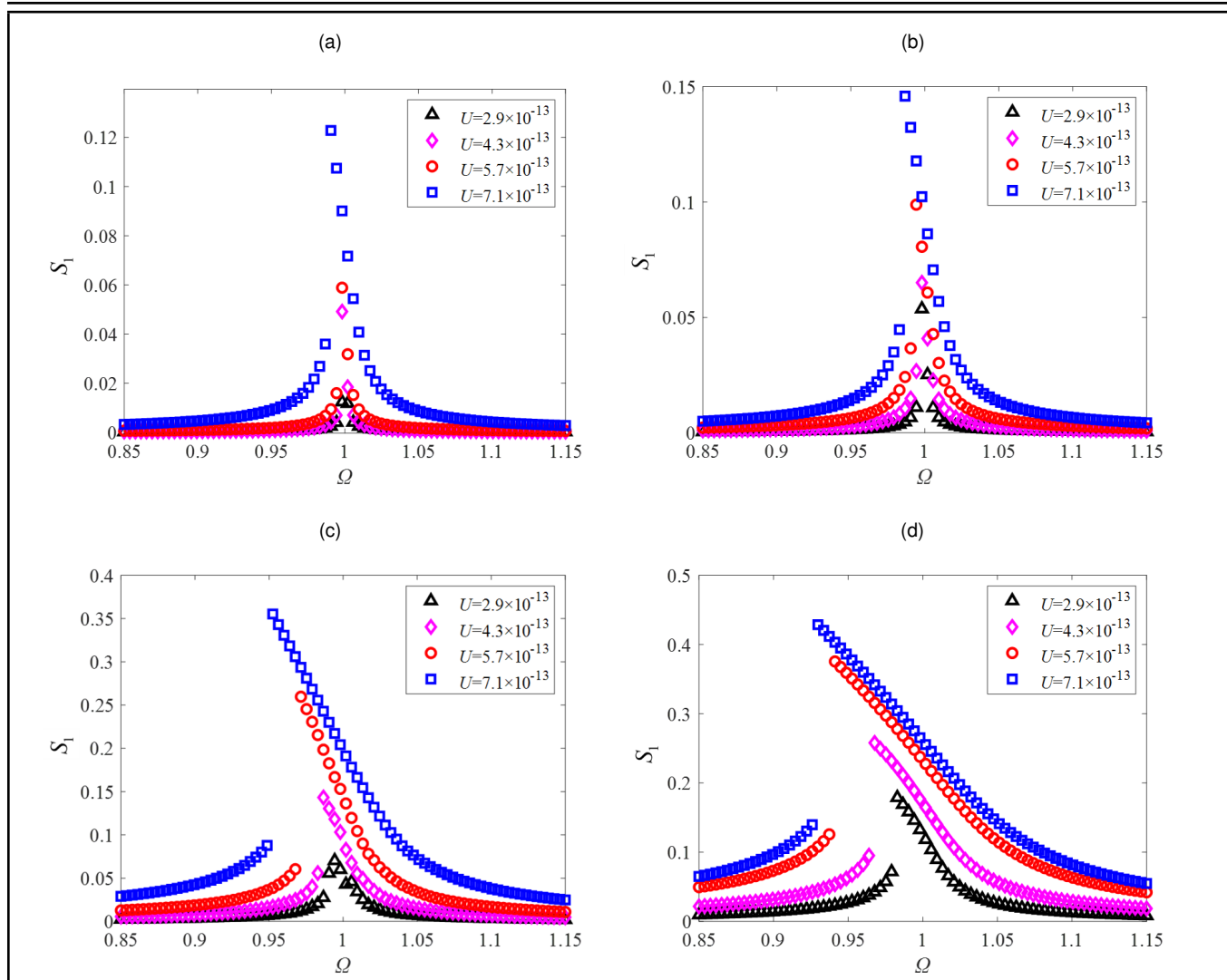


**Figure 9.** Amplitude frequency response curve of main resonance for different operating speeds: (a)  $\sigma/R = 4.65 \times 10^{-7}$ , (b)  $\sigma/R = 6.98 \times 10^{-7}$ , (c)  $\sigma/R = 9.3 \times 10^{-7}$ , (d)  $\sigma/R = 1.16 \times 10^{-6}$ .

- 5 Kvarda, D., Galas, R., Omasta, M., Shi, L.-B., Ding, H., Wang, W.-J., Krupka, I., and Hartl, M. Asperity-based model for prediction of traction in water-contaminated wheel-rail contact, *Tribology International*, **157**, 106900, (2021). <https://doi.org/10.1016/j.triboint.2021.106900>
- 6 Xie, G. and Iwnicki, S. D. Simulation of wear on a rough rail using a time-domain wheel-track interaction model, *Wear*, **265** (11), 1572–1583, (2008). <https://doi.org/10.1016/j.wear.2008.03.016>
- 7 Rovira, A., Roda, A., Marshall, M. B, Brunskill, H., and Lewis, R. Experimental and numerical modelling of wheel-rail contact and wear, *Wear*, **271** (5), 911–924, (2011). <https://doi.org/10.1016/j.wear.2011.03.024>
- 8 Chen, H., Ban, T., Ishida, M., and Nakahara, T. Adhesion between rail/wheel under water lubricated contact, *Wear*, **253**, 75–81, (2002). [https://doi.org/10.1016/S0043-1648\(02\)00085-6](https://doi.org/10.1016/S0043-1648(02)00085-6)
- 9 Trummer, G., Buckley-Johnstone, L. E., Voltr, P., Meierhofer, A., Lewis, R., and Six, K. Wheel-rail creep force model for predicting water induced low adhesion phenomena, *Tribology International*, **109**, 409–415, (2017). <https://doi.org/10.1016/j.triboint.2016.12.056>
- 10 Shi, L. B., Ma, L., Guo, J., Liu, Q. Y., Zhou, Z. R., and Wang, W. J. Influence of low temperature environment on the adhesion characteristics of wheel-rail contact, *Tribology International*, **127**, 59–68, (2018). <https://doi.org/10.1016/j.triboint.2018.05.037>
- 11 Chang, C., Chen, B., Cai, Y., and Wang, J. An experimental study of high speed wheel-rail adhesion characteristics in wet condition on full scale roller rig, *Wear*, **440–441**, 203092, (2019). <https://doi.org/10.1016/j.wear.2019.203092>
- 12 Ishizaka, K., White, B., Watson, M., Lewis, S. R., and Lewis, R. Influence of temperature on adhesion coefficient and bonding strength of leaf films: A twin disc study, *Wear*, **454–455**, 203330, (2020). <https://doi.org/10.1016/j.wear.2020.203330>
- 13 White, B. and Lewis, R. Simulation and understanding the wet-rail phenomenon using twin disc testing, *Tribology International*, **136**, 475–486, (2019). <https://doi.org/10.1016/j.triboint.2019.03.067>
- 14 Baek, K.-S., Kyogoku, K., and Nakahara, T. An experimental study of transient traction characteristics between rail and wheel under low slip and low

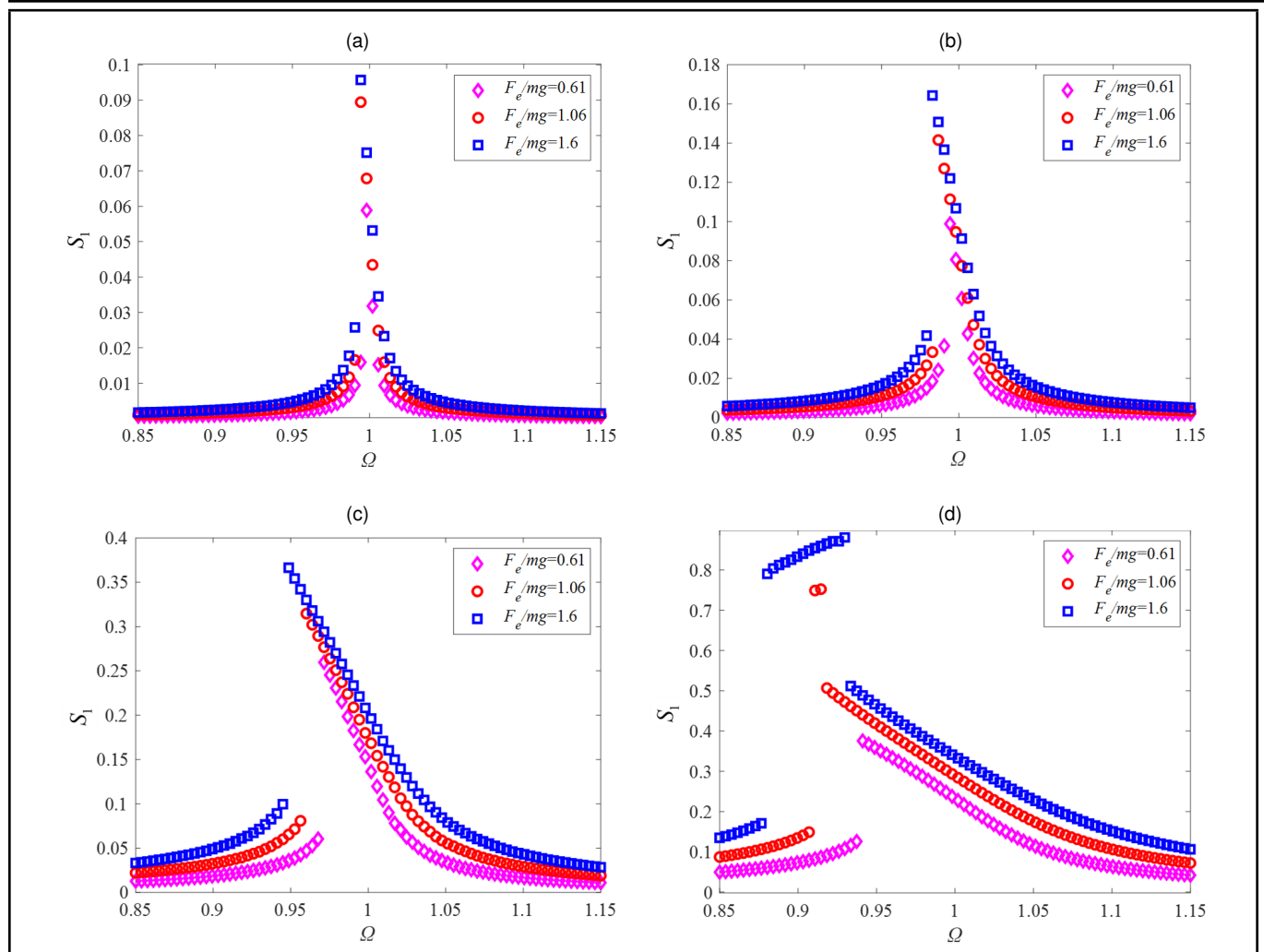


**Figure 10.** Amplitude frequency response curve of main resonance under different excitation loads: (a)  $\sigma/R = 4.65 \times 10^{-7}$ , (b)  $\sigma/R = 6.98 \times 10^{-7}$ , (c)  $\sigma/R = 9.3 \times 10^{-7}$ , (d)  $\sigma/R = 1.16 \times 10^{-6}$ .

speed conditions, *Wear*, **265** (9), 1417–1424, (2008). <https://doi.org/10.1016/j.wear.2008.02.044>

<sup>15</sup> Liu, X., Xiao, C., and Meehan, P. A. The effect of rolling speed on lateral adhesion at wheel/rail interface under dry and wet condition, *Wear*, **438–439** (2), 203073, (2019). <https://doi.org/10.1016/j.wear.2019.203073>

<sup>16</sup> Rong, K. J., Xiao, Y. L., Shen, M. X., Zhao, H. P., Wang, W. J., and Xiong, G. Y. Influence of ambient humidity on the adhesion and damage behavior of wheel–rail interface under hot weather condition, *Wear*, **486–487**, 204091, (2021). <https://doi.org/10.1016/j.wear.2021.204091>

<sup>17</sup> Galas, R., Omasta, M., Shi, L. B., Ding, H., Wang, W. J., Krupka, I., and Hartl, M. The low adhesion problem: The effect of environmental conditions on adhesion in rolling-sliding contact, *Tribology International*, **151**, 106521, (2020). <https://doi.org/10.1016/j.triboint.2020.106521>

<sup>18</sup> Wu, B., Wen, Z., Wang, H., Jin, X. Numerical analysis on wheel/rail adhesion under mixed contamination of oil and water with surface roughness, *Wear*, **314** (1–2), 140–147, (2013). <https://doi.org/10.1016/j.wear.2013.11.041>

<sup>19</sup> Wu, B., Wen, Z., Wang, H., and Jin, X. Analysis of wheel/rail adhesion under oil contamination with surface roughness, *Proceedings of the Institution of Mechanical Engineers, Part J: Journal of Engineering Tribology*, **227** (11), 1306–1315, (2013). <https://doi.org/10.1177/1350650113491866>

<sup>20</sup> Wu, B., Wu, T., Wen, Z., and Jin, X. Numerical analysis of high-speed wheel/rail adhesion under interfacial liquid contamination using an elastic-plastic asperity contact model, *Proceedings of the Institution of Mechanical Engineers, Part J: Journal of Engineering Tribology*, **231** (1), 63–74, (2017). <https://doi.org/10.1177/1350650116645025>

<sup>21</sup> Greenwood, J. A. and Williamson, J. Contact of nominally flat surfaces, *Proceedings of the Royal Society of London*, **295** (1442), 300–319, (1966). <https://doi.org/10.1098/rspa.1966.0242>

<sup>22</sup> Xiao, H., Sun, Y., and Xu, J. Investigation into the normal contact stiffness of rough surface in line contact mixed elastohydrodynamic lubrication, *Tribology Transactions*, **61**, 742–753, (2018). <https://doi.org/10.1080/10402004.2017.1404177>

<sup>23</sup> Yang, F., Wei, Z. L., Sun, X. F., Shen, C., and Núñez, A. Wheel-rail rolling contact behavior induced by both rail surface irregularity and sleeper

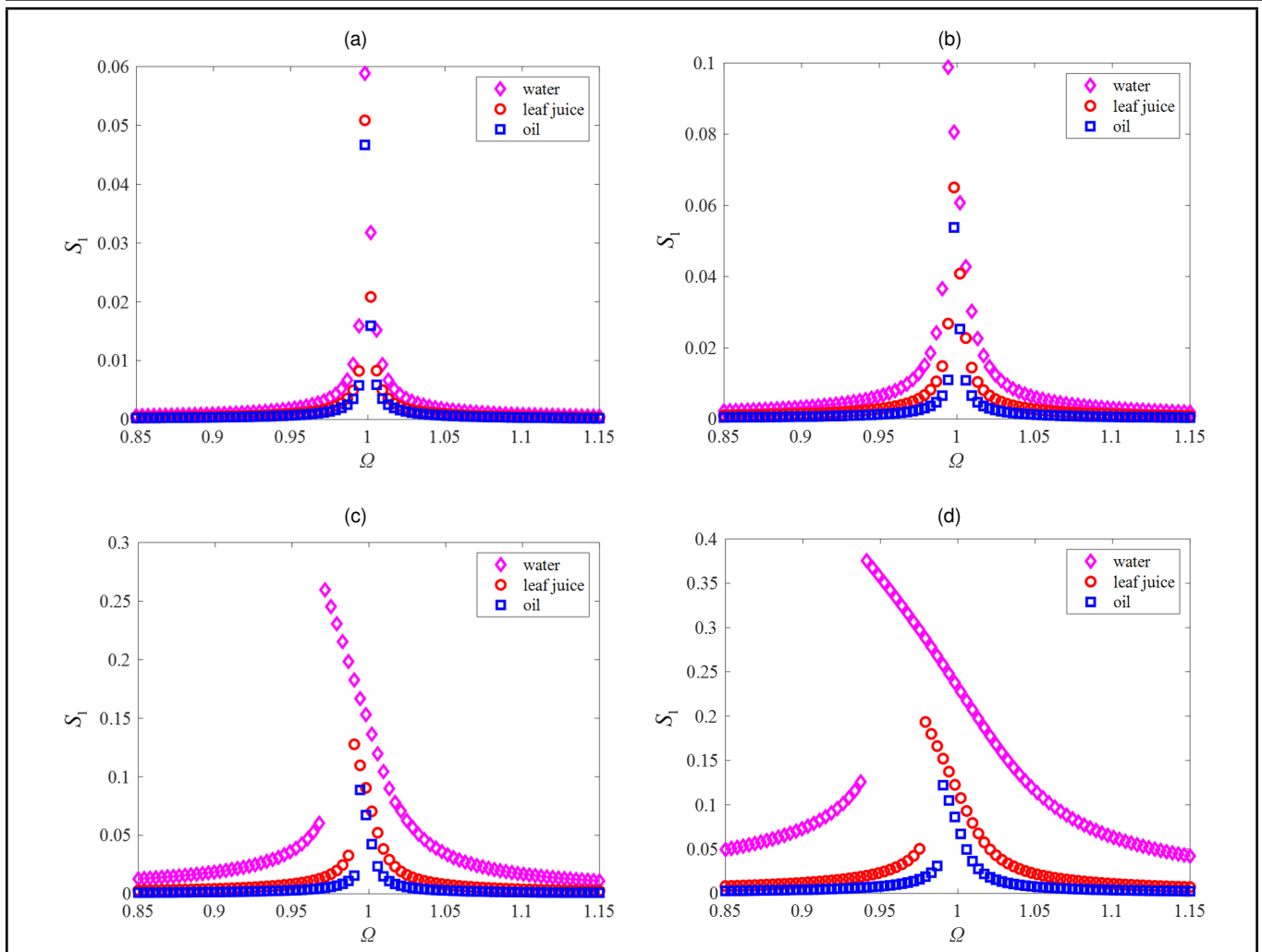


**Figure 11.** Amplitude frequency response curve of main resonance under different liquid medium: (a)  $\sigma/R = 4.65 \times 10^{-7}$ , (b)  $\sigma/R = 6.98 \times 10^{-7}$ , (c)  $\sigma/R = 9.3 \times 10^{-7}$ , (d)  $\sigma/R = 1.16 \times 10^{-6}$ .

hanging defects on a high-speed railway line, *Engineering Failure Analysis*, **128**, 105604, (2021). <https://doi.org/10.1016/j.engfailanal.2021.105604>

<sup>24</sup> Masjedi, M. and Khonsari, M. M. On the effect of surface roughness in point-contact EHL: Formulas for film thickness and asperity load, *Tribology International*, **134** (1), 011503, (2012). <https://doi.org/10.1016/j.triboint.2014.09.010>

<sup>25</sup> Xiao, H. and Sun, Y. On the normal contact stiffness and contact resonance frequency of rough surface contact based on asperity micro-contact statistical models, *European Journal of Mechanics—A/Solids*, **75**, 450–460, (2019). <https://doi.org/10.1016/j.euromechsol.2019.03.004>

<sup>26</sup> Bush, A. W., Gibson, R. D., and Keogh, G. P. Strongly anisotropic rough surfaces, *Journal of Tribology*, **101** (1), 15–20, (1979). <https://doi.org/10.1115/1.3453271>

<sup>27</sup> Serest, A. E. and Akbarzadeh, S. Mixed-elastohydrodynamic analysis of helical gears using load-sharing concept, *Proceedings of the Institution of Mechanical Engineers, Part J: Journal of Engineering Tribology*, **228** (3), 320–331, (2014). <https://doi.org/10.1177/1350650113506571>

<sup>28</sup> Liu, C., Xu, J., Wang, K., Liao, T., and Wang, P. Numerical investigation on wheel-rail impact contact solutions excited by rail spalling failure, *Engineering Failure Analysis*, **135**, 106116, (2022). <https://doi.org/10.1016/j.engfailanal.2022.106116>

<sup>29</sup> Sun, Y., Xiao, H., Xu, J., and Yu, W. Study on the normal contact stiffness of the fractal rough surface in mixed lubrication, *Proceedings of the Institution of Mechanical Engineers, Part J: Journal of Engineering Tribology*, **232** (12), 135065011875874, (2018). <https://doi.org/10.1177/1350650118758741>

<sup>30</sup> Wang, L., Yang, Z., Yang, X., Wang, C., Huang, Y., and Deng, Q. Research on macro-mesoscopic normal dynamic characteristics of sliding joint surface, *Mechanical Systems and Signal Processing*, **113**, 156–167, (2018). <https://doi.org/10.1016/j.ymsp.2017.01.007>

<sup>31</sup> Nayfeh, A. H. and Mook, D. T. *Nonlinear Oscillations*, Wiley, New York, (1979).

<sup>32</sup> Wu, B., Xiao, G., An, B., Wu, T., and Shen, Q. Numerical study of wheel/rail dynamic interactions for high-speed rail vehicles under low adhesion conditions during traction, *Engineering Failure Analysis*, **137**, 106266, (2022). <https://doi.org/10.1016/j.engfailanal.2022.106266>